Applied Physics A (2023) 129:77
https://doi.org/10.1007/s00339-022-06346-7

Applied Physics A
Materials Science & Processing

Ferroelectric, ferromagnetic and magneto-capacitance properties of Sm-doped $BiFeO_3$-$BaTiO_3$ solid solution

Huihui Zhao[1] · Yangjun Lai[1] · Liansen Feng[1] · Jingdong Shen[1] · Xiyue Jia[1] · Wei Mi[1] · Qi Li[1]

Received: 30 August 2022 / Accepted: 18 December 2022 / Published online: 5 January 2023

Abstract
In the present investigation, Sm-modified solid solutions of $BiFeO_3$-$BaTiO_3$ (BFO-BTO) have been synthesized using a solid-state reaction route. All ceramics sintered at 980 °C for 2 h possess a pure perovskite structure. XRD patterns show that the coexistence of rhombohedral and orthorhombic phases is found at $x = 0.01$–0.04. The average grain size increases with x up to 0.06. The ferroelectric, ferromagnetic and magneto-capacitance properties of the system are both effectively improved under Sm substitution. The hybridization strength between Bi 6*sp* and O 2*p* increases under Sm substitution, leading to the enhancement of the ferroelectric properties of the system. From Fe $L_{2,3}$- edge spectra, the hybridization strength of O 2*p* with Fe 3*d* decreases, resulting in the improvement of magnetization under Sm substitution in BFO-BTO.

Keywords Multiferroic ceramics · Magnetoelectric coupling · X-ray absorption spectroscopy · Hybridization

1 Introduction

In recent years, multiferroic materials, exhibiting simultaneously the ferroelectric and magnetic order, have been widely investigated due to their potential applications in various advanced devices, such as data storage, actuators, sensors and ultra-high speed telecommunication devices. $BiFeO_3$ (BFO) is one of the multiferroic materials that exhibit the coexistence of ferroelectric and magnetic properties in perovskite structures at room temperature in the same phase. BFO with a rhombohedral-distorted ABO_3-type perovskite structure (*R3c*) exhibits ferroelectricity with high Curie temperature ($T_C \sim 1103$ K). The G-type antiferromagnetic properties ($T_N \sim 643$ K) have recently attracted considerable attention [1, 2]. It possesses a large intrinsic polarization as high as ~ 90 μC/cm^2, which is ascribed to the distortion of FeO_6 octahedron caused by the presence of $6s^2$ lone pairs of electrons at the Bi site [3, 4]. However, various constraints restrict the applicability of BFO for practical applications, such as difficult to synthesize pure phase, low ferroelectric property, and high leakage current, etc. [5, 6]. To overcome these problems, many researchers mainly concentrate on the following methods to improve the performance of BFO, including modification of preparation methods (such as the fast liquid phase method [7], microwave method, sol–gel, etc.), the substitution of other ions at A or B sites [8, 9], and formation of solid solution with other ABO_3-type perovskite structure (such as $BaTiO_3$ (BTO) and $SrTiO_3$, etc.) to effectively inhibit the generation of impurity and improve the electrical insulativity, especially the solid solution formed with $BaTiO_3$ [10].

The (1-*x*)$BiFeO_3$-*x*$BaTiO_3$ (BFO-*x*BTO) ($0.3 \le x \le 0.4$) sample with a morphotropic phase boundary (MPB) with rhombohedral and cubic (or tetragonal) phases can obtain excellent ferroelectric and piezoelectric properties [11–13]. The BFO-*x*BTO ($0.10 \le x \le 0.25$) sample with a rhombohedral phase is obtained [12–15]. The chemical substitution (such as Cr, Co, Nd, Eu, etc.) at the Bi site in BFO-BTO has been investigated, showing the enhancement of magnetoelectric effect, ferroelectric, piezoelectric and magnetic properties due to structural distortion and partial destruction of spiral spin structure [16–20]. The rare-earth element substitution favors the formation of paraelectric orthorhombic phase [21]. The Sm substitution with a smaller ionic radius than Bi at the Bi sites in BFO leads to the improvement of the ferroelectric, piezoelectric and magnetic properties [22, 23]. The Sm-doped BFO undergoes structural transformation from rhombohedral to orthorhombic phase [22, 24, 25]. Therefore, in the present work, a solid solution of

✉ Qi Li
qli@seu.edu.cn

[1] School of Physics, Southeast University, Nanjing 211189, People's Republic of China

$0.79Bi_{1-x}Sm_xFeO_3$–$0.21BaTiO_3$ was fabricated by a traditional ceramic technique in air with the rhombohedral and orthorhombic phases. The effects of Sm doping on the microstructure, ferroelectric, ferromagnetic and magnetocapacitance properties of the ceramics were studied.

2 Materials and methods

In this paper, the $0.79Bi_{1-x}Sm_xFeO_3$-$0.21BaTiO_3$ (BFO-BTO-Sm-x) ceramics ($x = 0.00, 0.01, 0.03, 0.04, 0.06$) were successfully prepared by the traditional solid-state reaction method. Raw materials of Bi_2O_3 (99.9%), $BaCO_3$ (AR), Fe_2O_3 (99.9%), TiO_2 (99.8%) and Sm_2O_3 (99.99%) were used. The powders were stoichiometrically mixed according to the chemical formula and then ball-milled for 24 h at 450 rpm using ZrO_2 balls in a polymer jar with ethanol as a milling media. The mixed precursors were dried in an oven at 80 °C and calcined for 4 h at 800 °C. An additional ball-milling step was conducted for 24 h at 450 rpm following calcination to achieve better homogeneity of the final powders. The synthesized powders were mixed with a PVA binder solution, then pressed into disk samples at 10 MPa and dried at 650 °C for 3 h. Finally, the compacts were sintered at 980 °C for 2 h in air. Silver electrodes were treated on the top and bottom surfaces of the samples at 220 °C for 30 min.

The structural properties were studied using X-ray diffraction (XRD). The XRD patterns were recorded at room temperature using an X-ray powder diffractometer with Cu $K\alpha$ radiation. Room-temperature dielectric properties were measured by an impedance analyzer (Agilent 4284A). In a wide frequency range of 100 Hz to 1 MHz, the a.c. electrical conductivity and ferroelectric measurements were carried out as a function of the electric field using the ferroelectric test system TRI- Multiferroic 4 kV at room temperature. The magnetic measurements were performed by using a physical property measurement system (PPMS) at room temperature. X-ray absorption spectroscopy (XAS) of Fe $L_{2,3}$ and O K-edge were measured at the photoelectron station of Beijing Synchrotron Radiation Facility (BSRF), Beijing, China.

3 Results and discussion

The XRD patterns of BFO-BTO-Sm-x ($x = 0$, 0.01, 0.03, 0.04, 0.06) ceramics are shown in Fig. 1. This figure shows that all ceramics exhibit a pure perovskite structure. A small impurity phase was detected around 30°, suggesting that Ba^{3+}, Ti^{4+} and Sm^{3+} have diffused into the BFO lattices to form a homogenous solid solution. Similar to BFO, the sample of $x = 0$ exhibits a rhombohedral symmetry (*R3c,* JCPDS card 71–2494). As shown in Fig. 1b, it can be seen that the diffraction peaks at 2θ ~ 39° gradually change as x increases to 0.06. It suggests that a phase transition occurs after substitutions of Sm^{3+} for Bi^{3+}. The diffraction peak splitting at 2θ ~ 39° becomes more noticeable for $x = 0.03$ and 0.04, and then indistinct as x up to 0.06, indicating the coexistence of rhombohedral and orthorhombic (*Amm2*, JCPDS card 75–1608) phases for the samples with $x = 0.01 \sim 0.04$. Apart from the structural transition, the peak shifts to a higher angle under Sm substitution due to the smaller ion radius of Sm^{3+} (0.0995 nm) than that of Bi^{3+} (0.103 nm) at A sites. To characterize the phase compositions in the samples, the peaks at 38°–40.5° were fitted by the Gaussian function as shown in Fig. 2. The peaks between 38° and 40.5° were fitted to $(006)_R/(202)_R$ and $(102)_O/(120)_O$, where R and O denote rhombohedral and orthorhombic phases, respectively.

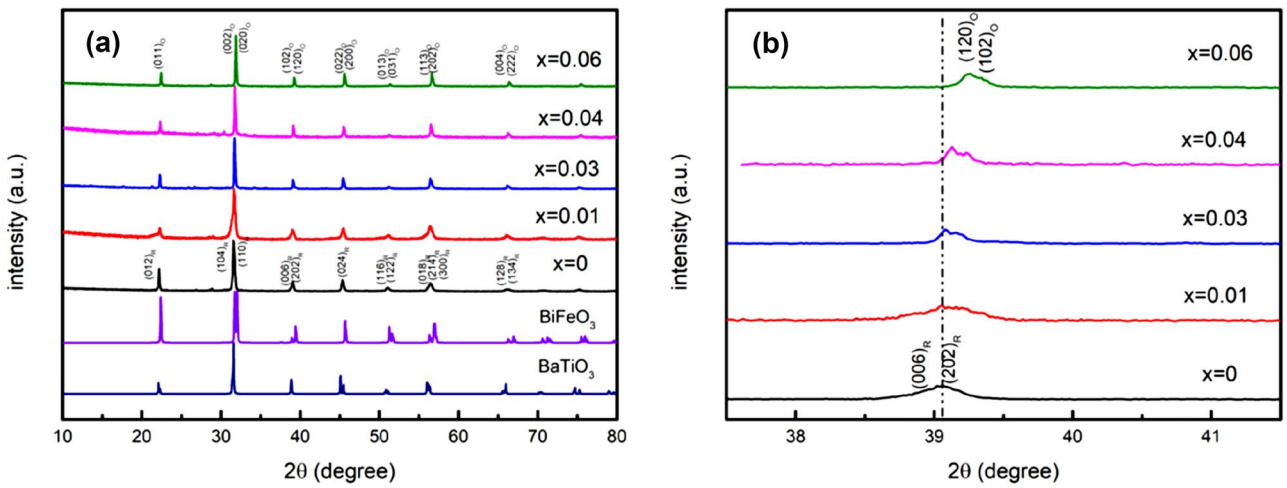

Fig. 1 XRD patterns of the BFO-BTO-Sm-x ($x = 0$, 0.01, 0.03, 0.04, 0.06) ceramics

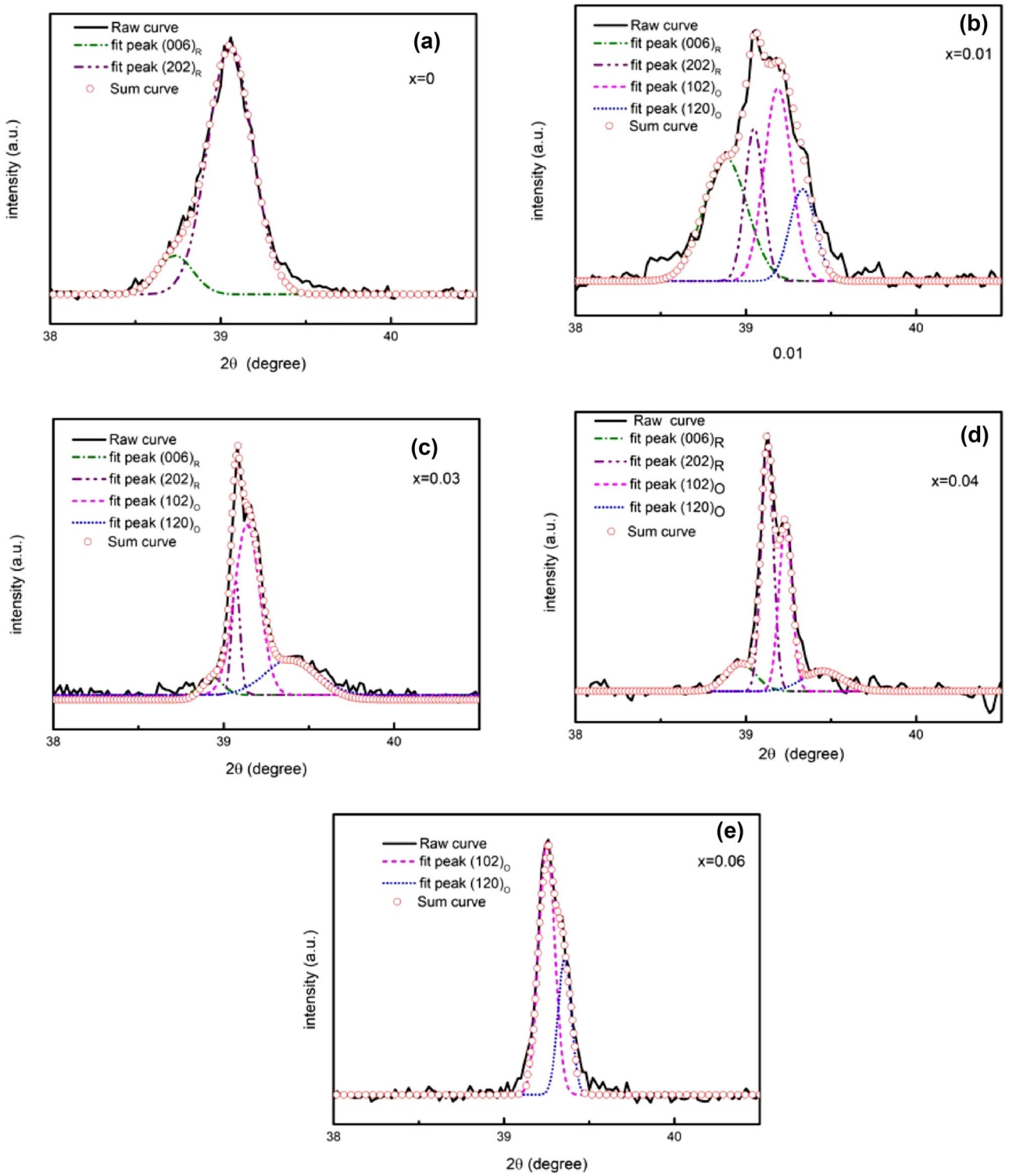

Fig. 2 XRD fitting patterns of the BFO-BTO-Sm-x ($x = 0$, 0.01, 0.03, 0.04, 0.06) ceramics in the 2θ ranges of 38°–40.5°

The ceramic with $x = 0$ shows a rhombohedral phase with the $(006)_R/(202)_R$ diffraction peaks as shown in Fig. 2a. As x increases, it shows the transformation from $(006)_R/(202)_R$ peaks to $(102)_O/(120)_O$ peaks. The ceramic with $x = 0.06$ shows an orthorhombic phase with $(006)_R/(202)_R$ diffraction peaks as shown in Fig. 2e. It indicates that the MPB of rhombohedral and orthorhombic phases is formed for the samples of $x = 0.01$–0.04.

Figure 3 shows the SEM images of BFO-BTO-Sm-x ($x=0$, 0.01, 0.03, 0.04, 0.06) ceramics. These images were taken from freshly fractured surfaces. The samples show inhomogeneous grain sizes as shown in Fig. 3. The grain size distributions for the samples calculated by nano-measurer software are shown in Fig. 4(a–e). The grain size distributions become more scattered. The average grain size and percentage of porosity are shown in Fig. 4f. The grain size decreases and the percentage of porosity increases under Sm substitution. It means that the electrical insulativity will change as the number of porosity varies in samples.

The *P-E* hysteresis loop is one of the most important characteristics of a ferroelectric material and gives information on its dynamic polarizability. Figure 5 shows the *P-E* loops for BFO-BTO-Sm-x ceramics at room temperature. It can be seen that all the samples show an obvious electrical hysteresis. The remnant polarization (P_r) as shown in Fig. 5f increases when $x \leq 0.04$, then decreases for higher Sm content at $x=0.06$. The maximum ferroelectric characterization is obtained with P_r of 3.83 μC/cm^2 and E_c of 4.01 kV/mm at $x=0.04$. The enhancement of ferroelectric properties is due to the formation of the MPB of rhombohedral and orthorhombic phases. The rhombohedral and orthorhombic phase possesses different spontaneous polarization directions [26], which may give more total polarizations when the two phases coexist.

Figure 6 shows the leakage current density J of the BFO-BTO-Sm-x ceramics. The leakage current can directly reflect

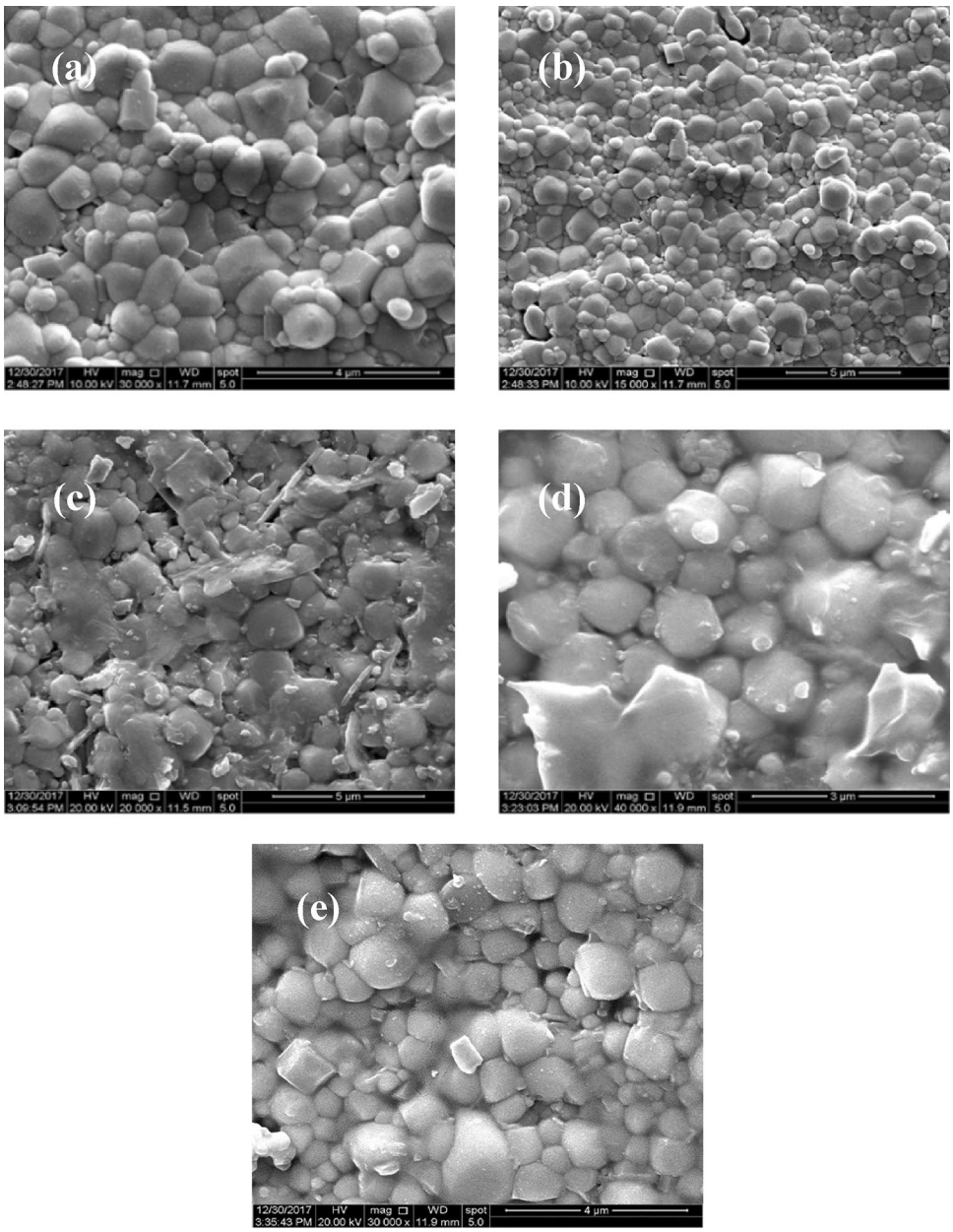

Fig. 3 SEM micrographs of the BFO-BTO-Sm-x ceramics sintered: **a** $x=0$, **b** $x=0.01$, **c** $x=0.03$, **d** $x=0.04$ and **e** $x=0.06$

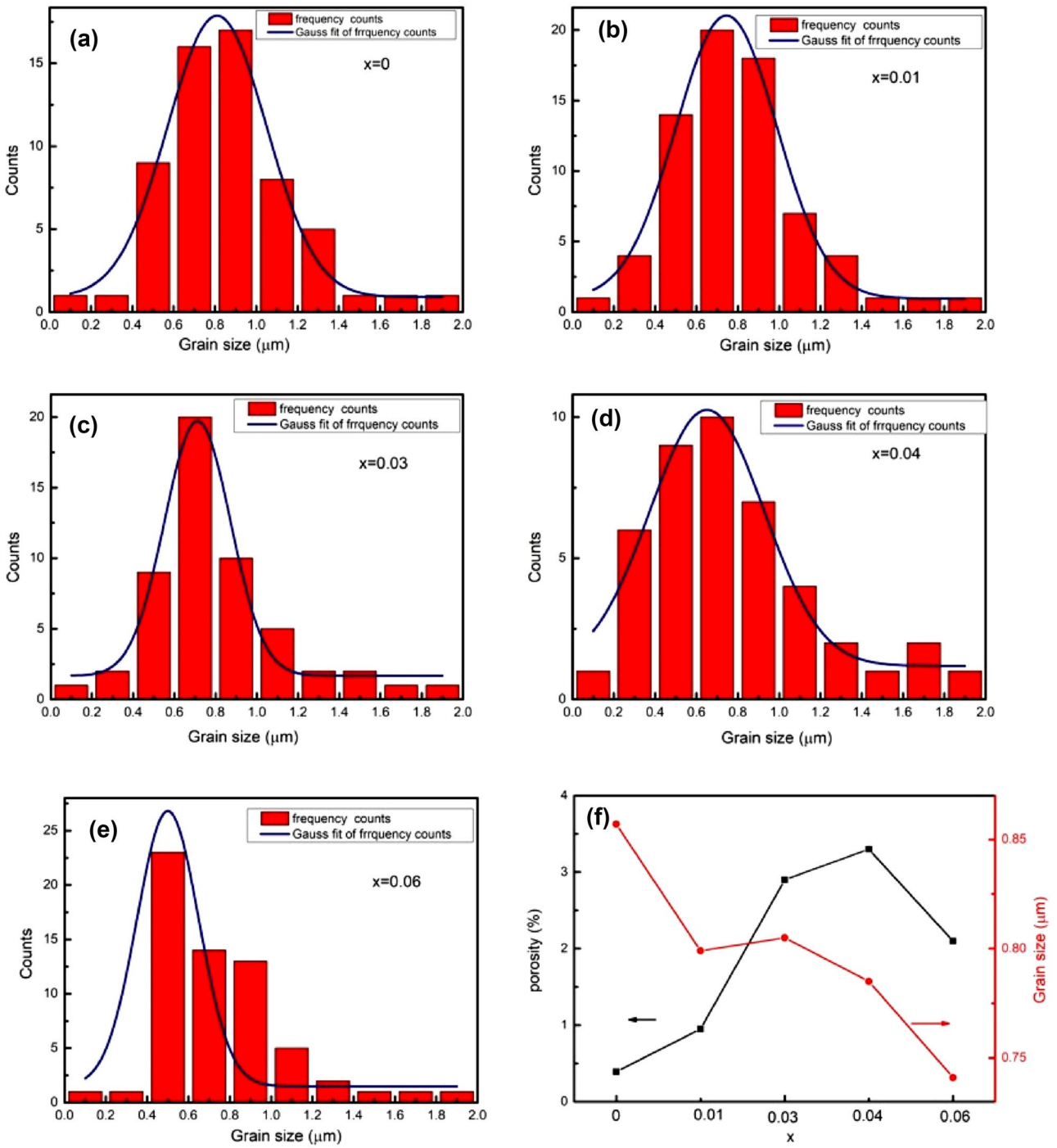

Fig. 4 (**a**–**e**) Grain size distribution of the BFO-BTO-Sm-x (x = 0, 0.01, 0.03, 0.04, 0.06) ceramics. **f** The average grain size and percentage of porosity of the BFO-BTO-Sm-x ceramics

the insulativity of samples. The larger the leakage current is, the smaller the resistance is for the samples as shown in Fig. 6(a, b). It plays an important role in multiferroic properties and piezoelectric properties. It can be seen that all ceramics exhibit lower J values of 1.77×10^{-7}-1.16×10^{-5} (A/cm^2) under an electric field of 40 kV/cm than that of pure BFO ceramic (8.18×10^{-4} (A/cm^2)), suggesting that all ceramics exhibit better electrical insulativity [5]. The high leakage current in BFO is attributed to the presence of charged oxygen vacancies for charge compensation and the reduction of Fe^{3+} to Fe^{2+} during sintering [5]. The lower leakage current of BFO-BTO than that of BFO is due to the

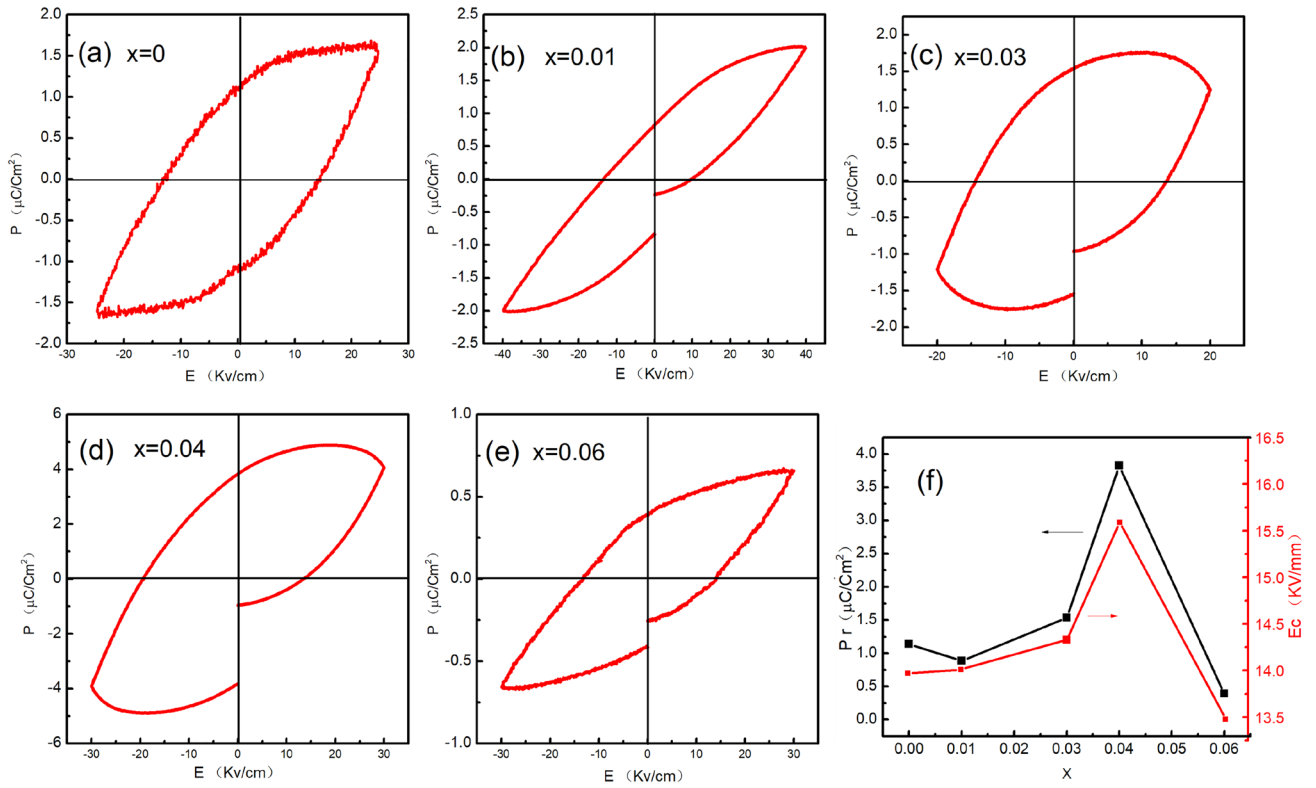

Fig. 5 (**a**–**e**) Ferroelectric hysteresis loops for different x in BFO-BTO-Sm-x ceramics at $x = 0.0$–0.06. **f** The variation of polarization (P_r) and electric field (E_C) for BFO-BTO-Sm-x ceramics

suppression of the reduction of Fe ions from Fe^{3+} to Fe^{2+} leading to the decrease of oxygen vacancies [27]. With the increase of x, the leakage current density becomes larger than that of pure BFO-BTO, which indicates that the insulativity of the BFO-BTO system can be inhibited under Sm substitution. It suggests that both the reduction of Fe ions from Fe^{3+} to Fe^{2+} and oxygen vacancies increase under Sm substitution in BFO-BTO. To further understand the conduction mechanism, the logarithmic plots of J-E and its fitting curves are presented in Fig. 6c. After fitting, the log$J$-log$E$ curves show a linear relationship. The slope of the fitting curves at low voltage is close to 1.0, indicating that the conduction mechanism follows Ohm's law. The slight drift at high voltage is attributed to the space-charge-limited conduction (SCLC) [25].

The magnetic hysteresis loops of BFO–BTO–Sm-x ceramics are presented in Fig. 7. The undoped BFO-BTO sample exhibits a partially saturated and weak hysteresis with M_s of 0.504 emu/g and coercive field ($H_C = 1826$ Oe). With the increase of x, the hysteresis loop gradually becomes more saturated, and the saturation magnetization M_s increases rapidly and reaches the maximum at $x = 0.03$ with the value of 3.43 emu/g; when $x > 0.03$, the saturation magnetization M_s gradually decreases to 2.45 emu/g at $x = 0.06$. This change of magnetic properties may be associated with the structural distortion. It is well known that BFO possesses a distorted rhombohedral structure and a G-type antiferromagnetic spin spiral structure [4]. This structure also suppresses the macroscopic magnetization, resulting in the inability to observe the large magnetoelectric effect. The spiral structure might be further distorted, leading to the release of more suppressed magnetization. The sample of $x = 0.03$ possesses the highest M_S because it is in the coexistence state of rhombohedral and orthorhombic phases. In BFO-$SrTiO_3$ and BFO-BTO materials, a similar correlation between crystal symmetry and ferromagnetism has also been reported [28, 29]. The enhanced magnetization of the Sm-doped samples will be interesting for magnetic field sensor applications.

Figure 8a shows the frequency variations of the dielectric constant for BFO-BTO-Sm-x ceramics from 100 Hz to 1 MHz frequency. It can be seen that the values of the dielectric constant decrease with increasing frequency. The observation has been explained by the phenomenon of dipole relaxation wherein at low frequencies the dipoles are able to follow the frequency of the applied field [27]. It can be seen that the dielectric constant of pure BFO-BTO is higher than that of the ceramics at $x = 0.01$ and 0.06, and the dielectric constant of the ceramics at $x = 0.03$ and 0.04 is higher than that of pure BFO-BTO. The highest dielectric constant is at

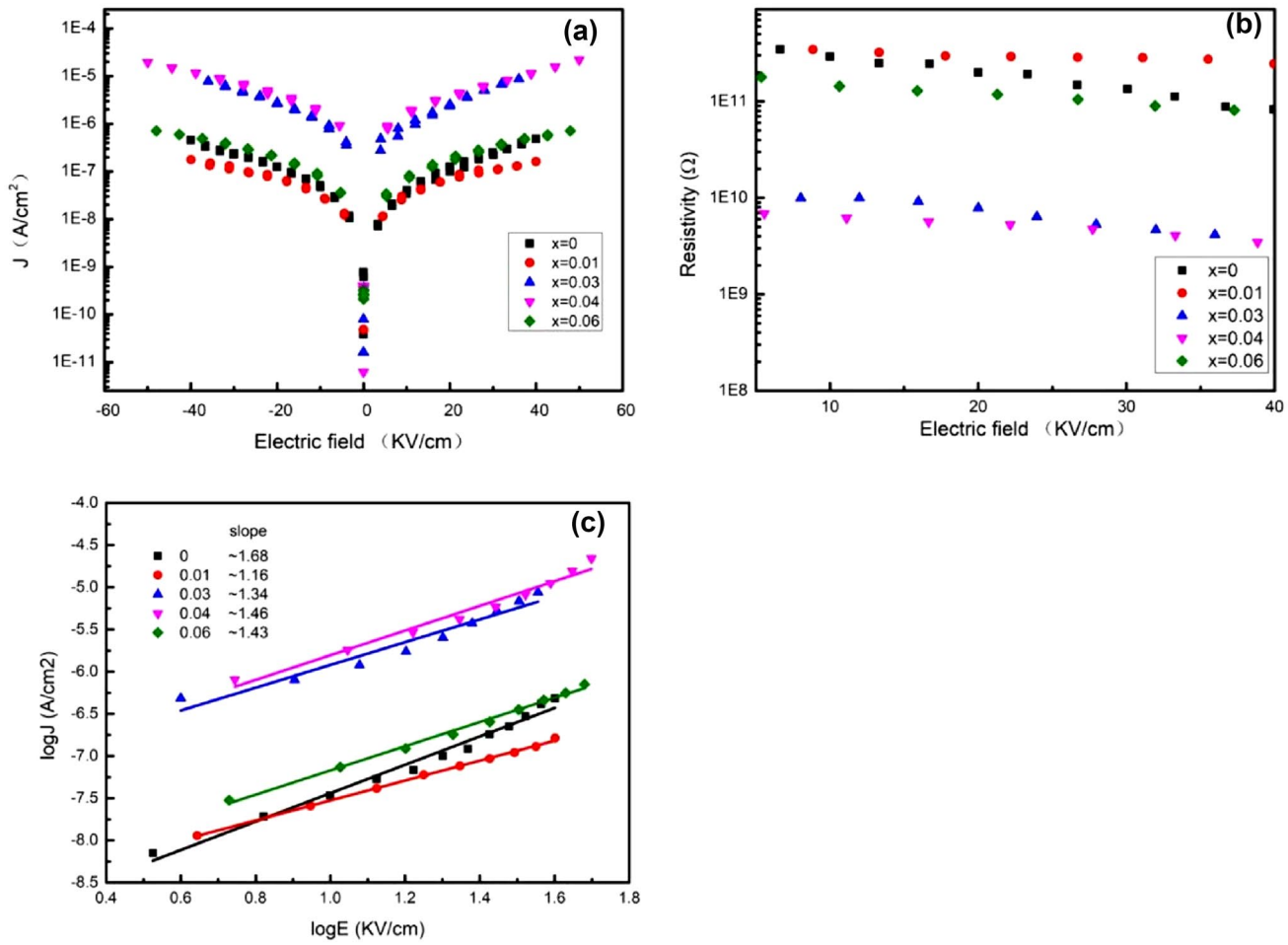

Fig. 6 a Leakage current density J of the BFO-BTO-Sm-x ($x=0$, 0.01, 0.03, 0.04, 0.06) ceramics; **b** resistivity vs. electric field of the BF-BT-Sm-x ceramics; **c** double logarithmic scale log J vs log$E$ fitted of the BF-BT-Sm-x ceramics

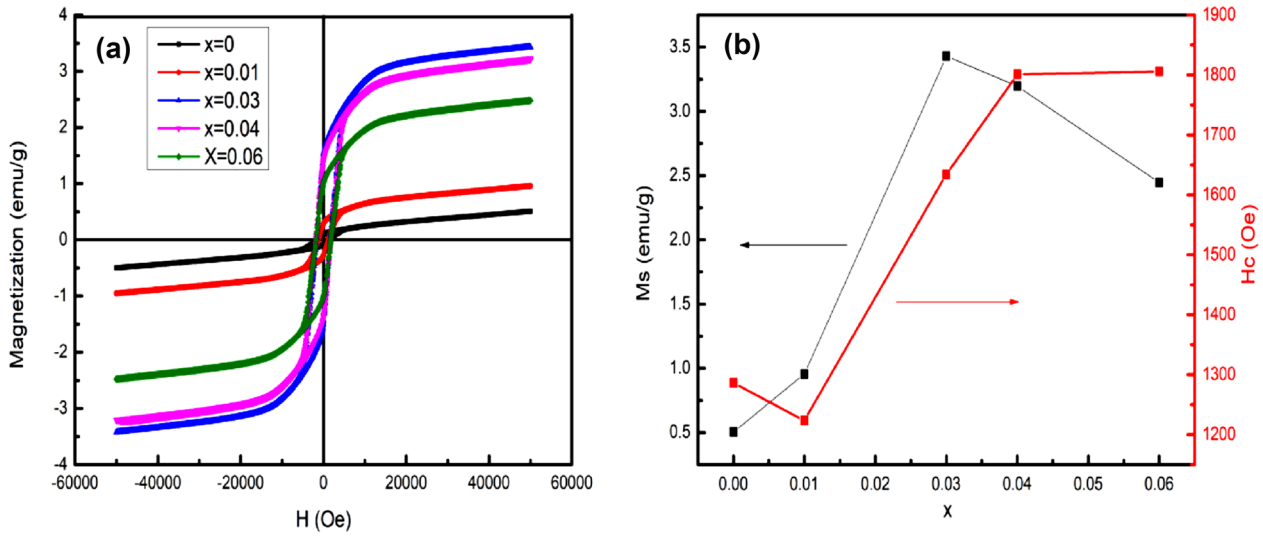

Fig. 7 (**a**–**e**) M–H loops of BFO-BTO-Sm-x ceramics measured at room temperature; **(f)** variations of saturated magnetization M_s and coercive field H_c of the BFO-BT-Sm-x ceramics

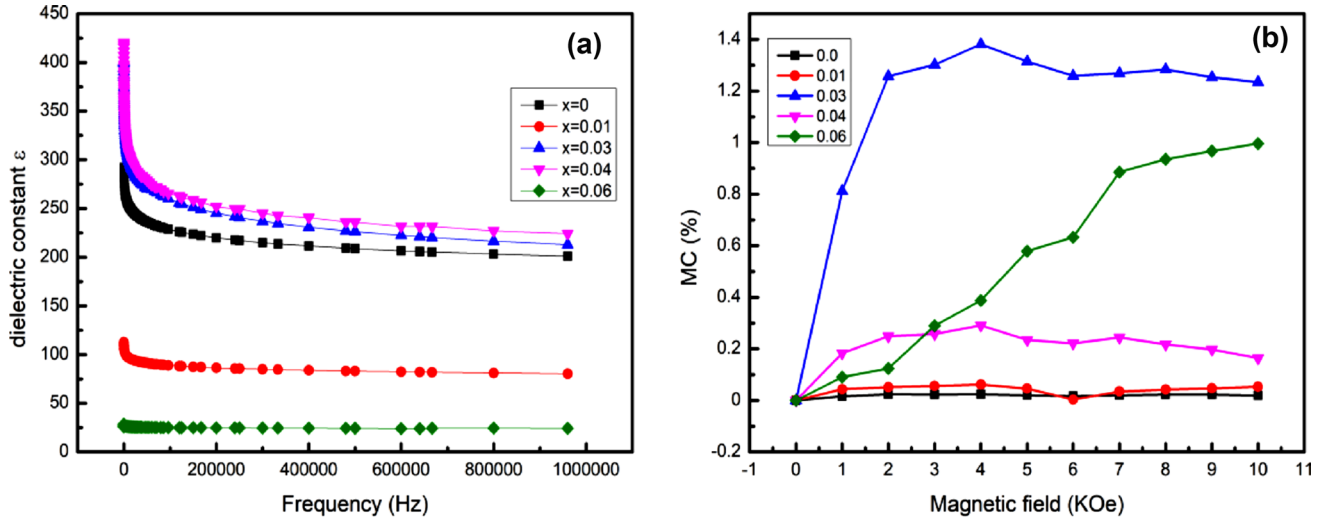

Fig. 8 a Dielectric constant of BFO-BTO-Sm-x (x = 0–0.06) ceramics at room temperature. **b** The magneto-capacitance of BFO-BTO-Sm-x ceramic with the different magnetic fields at 5 kHz

x = 0.04, which is consistent with the P-E loops. Figure 8b shows the magneto-capacitance of BFO-BTO-Sm-x ceramics with different magnetic fields. The magnetoelectric effect is a known property in most of multiferroics induced by the coupling between electrical and magnetic dipoles. A magnetoelectric material gets strained after the application of a magnetic field. This strain induces stress in the material. This stress generates an electric field on the ferroelectric domains, leading to a modification of the dielectric constant [30]. The change rate of dielectric constant under different magnetic field intensities can indirectly characterize the magnetoelectric coupling effect between electrical and magnetic dipoles. Magneto-capacitance (MC) is defined as the change in dielectric constant (ε_r) value with an external magnetic field. It is also a sign of the magnetoelectric properties of a multiferroic material. Its mathematical expression is,

$$MC(\%) = \frac{\varepsilon_r(H) - \varepsilon_r(0)}{\varepsilon_r(0)} \times 100\%$$

where $\varepsilon_r(H)$ and $\varepsilon_r(0)$ denote dielectric constants at applied magnetic field H and zero fields, respectively [30, 31]. The values of MC for Sm-substituted BFO-BTO ceramics are higher than that of BFO-BTO under the magnetic field of 10 kOe. The value of MC increases to 1.3% at x = 0.03 and then decreases to 0.16% at x = 0.04. It is noted that the sample for x = 0.03 owns a best-saturated magnetization M_s and better residual polarization P_r, showing stronger magnetoelectric coupling. As x up to 0.06, the value of MC increases to 0.99%, where the crystal structure just deviates from the MPB. The high resistivity and low leakage current lead to the large strain and energy transfer requisite for an enhanced magnetoelectric coupling [32–34]. Due to the structural transformation from rhombohedral to orthorhombic, the destruction of spiral spin structure leads to the enhancement of magnetic properties [22, 35, 36]. Thus, the magnetoelectric coupling of x = 0.06 sample with lower leakage current and without $R3c$ phase is stronger than that of x = 0.04 sample. It indicates that the magnetoelectric coupling enhances under Sm substitution.

Figure 9 shows the O K-edge XAS spectra corresponding to the transition from O 1 s to 2p transition hybridized with the unoccupied Fe 3d, Bi 6 s/6p, and Sm 4f orbitals [37, 38]. The O K-edge absorption consists of two regions at ~ 530–536 eV (A and B) and ~ 536–545 eV (C and D). For $BiFeO_3$, the Fe ions generally have two states $3d^5(Fe^{3+})$ and $3d^6(Fe^{2+})$. The O 2p hybridized with the unoccupied

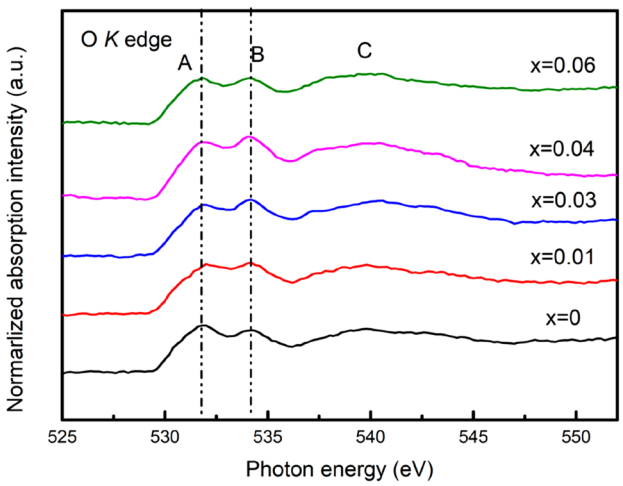

Fig. 9 O K-edge synchrotron XAS spectra of BFO-BTO-Sm-x (x = 0–0.06) ceramics

Fe 3*d* has mostly 3d characters and splits into t_{2g} and e_g bands by ligand field [39, 40]. The peak A corresponds to the hybridization of O 2*p* with unoccupied Fe 3*d*. The peak B can be attributed to the hybridization of O 2*p* with Bi 6 *s*/6*p* orbitals [41, 42]. The intensity of peak B increases with the increase of Sm content, indicating the increase of hybridization strength of O 2*p*–Bi 6 *s*/6*p* orbitals as the system approaches the MPB. The Bi 6*p*-O 2*p* hybridization is the main origin of *FE* polarization due to the off-center displacement of the Bi ions in $BiFeO_3$ [43]. The improvement of Bi 6 *s*/6*p*-O 2*p* hybridization leads to the enhancement of local *FE* polarization. The peak C centered at ~ 542 eV corresponds to the hybridizations of O 2*p* with the unoccupied Fe 4 *s*/4*p*, Sm 5*d*, and Bi 6*d* orbitals [38, 44–46]. The peak C of Sm-substituted BFO-BTO ceramics is broader than that of pure BFO-BTO. The broadness of XAS lines is recognized as an intrinsic property of oxygen vacancies [47, 48]. It indicates that oxygen vacancies increase in amount under Sm substitution,

Figure 10 displays the normalized Fe $L_{2,3}$-edge XAS spectra, due to the transitions from the Fe $2p_{3/2}$ to the unoccupied Fe 3*d* orbitals [49]. In the FeO_6 octahedron, the coupling between the Fe 3*d* and the O 2*p* orbitals causes a splitting of the fivefold degeneracy into triple-degenerate t_{2g} orbitals (lower photon energy) and double-degenerate e_g orbitals (higher photon energy) [50]. The energy gap between t_{2g} and e_g bands is ~ 1.4 eV. To determine the transformation of Fe^{3+} to Fe^{2+} for the BFO-BTO sample, the Fe $L_{2,3}$-edge XAS spectra of Fe^{3+} and Fe^{2+} obtained by calculation using CTM4XAS are presented in Fig. 10a. It can be seen that Fe ions in the BFO-BTO sample coexist in the form of bi- and tri-valence. As shown in Fig. 10b, the intensity of t_{2g} increases with the increase of Sm content, indicating that the ratio of the amount of Fe^{3+} to Fe^{2+} decreases. The increase of t_{2g} suggests the increase of the unoccupied state of Fe 3*d*, resulting in the reduction of the charge transfer between Fe 3*d* and O 2*p*. It suggests that the hybridization between Fe 3*d* and O 2*p* decreases. The enhancement of magnetic property can be caused by the existence of the double-exchange interaction of Fe^{3+}-O-Fe^{2+} due to the creation of Fe^{2+} [51, 52]. Thus, the decrease of hybridization of O 2*p* with unoccupied Fe 3*d* results in the improvement of magnetization.

4 Conclusions

In this paper, the $0.71Bi_{1-x}Sm_xFeO_3$-$0.29BaTiO_3$ ($x = 0$, 0.01, 0.03, 0.04, 0.06) solid solution ceramic samples were successfully prepared. Through the analysis of the XRD structure, it was found that the method of introducing $BaTiO_3$ and $BiFeO_3$ to form a solid solution could greatly inhibit the impurity phase in the process of $BiFeO_3$ preparation. XRD patterns show that the coexistence of rhombohedral and orthorhombic phases was formed at $x = 0.01$–0.04, called MPB structure. The better residual polarization $P_r = 3.83$ μC/cm^2 ($x = 0.04$) and the maximum saturation magnetization 3.43 emu/g ($x = 0.03$) are obtained near the MPB, so that we can observe the apparent magneto-dielectric coupling effect in the sample of $x = 0.03$, and the magneto-capacitance is as high as ~ 1.3%, the ferroelectric properties of the system can be effectively improved, especially the ferromagnetic properties have been greatly improved under Sm substitution. When the structure is close to MPB, the hybridization strength between Bi 6*sp* and O 2*p* increases, thus the ferroelectric properties of the system are improved. From Fe $L_{2,3}$- edge XAS spectra, the intensity of t_{2g} increases as Sm

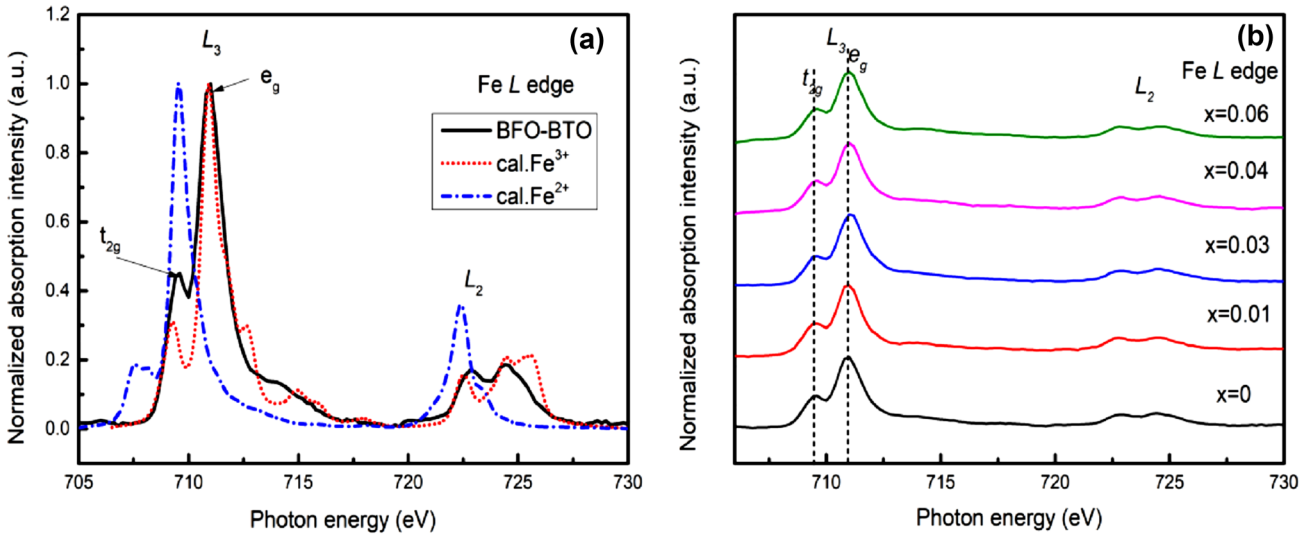

Fig. 10 Fe-$L_{3,2}$ edge synchrotron XAS spectra of (**a**) BFO and BFO-BTO, and (**b**) BFO-BTO-Sm-*x* ($x = 0$–0.06) ceramics

content increases, indicating that the hybridization strength of O 2*p* with Fe 3*d* decreases. The reduced hybridization results in the improvement of magnetization. It indicates that the system has potential application in the field of information storage for new devices.

Acknowledgements This work is supported by the open research fund of the Key Laboratory of MEMS of the Ministry of Education, Southeast University. We also gratefully acknowledge the support from the photoelectron spectroscopy station, Beijing Synchrotron Radiation Facility for the supplied beamtime, and the support from the Analysis and Testing Center of Southeast University for the XPS experiments.

Data availability Data for this manuscript are all available if required.

References

1. P. Fischer, M. Polomska, I. Sosnowska, M. Szymanski, J. Phys. C: Solid State Phys. **13**, 1931 (1980)
2. F. Kubel, H. Schmid, Acta. Cryst. B **46**, 698 (1990)
3. F. Yan, T.J. Zhu, M.O. Lai, L. Lu, Scripta Mater. **63**, 780 (2010)
4. G. Catalan, J.F. Scott, Adv. Mater. **21**, 2463 (2009)
5. S.K. Pradhan, B.K. Roul, Phys. B: Condens. Matter **406**, 3313 (2011)
6. A. Ravalia, M. Vagadia, P. Trivedi, P.S. Solanki, K. Asokan, S. Ojha, O.P. Thakur, R.J. Choudhary, D.M. Phase, D.G. Kuberkar, Solid State Commun. **169**, 10 (2013)
7. Y.P. Wang, L. Zhou, M.F. Zhang, X.Y. Chen, J.-M. Liu, Z.G. Liu, Appl. Phys. Lett. **84**, 1731 (2004)
8. Q. Li, S. Bao, Y. Liu, Y. Li, Y. Jing, J. Li, J. Alloy. Compds. **682**, 672 (2016)
9. P.K. Jha, P.A. Jha, P. Singh, R. Ranjan, R.K. Dwivedi, Phys. Chem. Chem. Phys. **19**, 26285 (2017)
10. H. Singh, A. Kumar, K.L. Yadav, Mater. Sci. Eng.: B **176**, 540 (2011)
11. D. Damjanovic, Appl. Phys. Lett. **97**, 062906 (2010)
12. H. Zhang, W. Jo, K. Wang, K.G. Webber, Ceram. Int. **40**, 4759 (2014)
13. B. Xun, A. Song, J. Yu, Y. Yin, J.-F. Li, B.-P. Zhang, A.C.S. Appl, Mater. Inter. **13**, 4192 (2021)
14. S. Kim, G.P. Khanal, H.-W. Nam, I. Fujii, S. Ueno, C. Moriyoshi, Y. Kuroiwa, S. Wada, J. Appl. Phys. **122**, 164105 (2017)
15. T. Zheng, J. Wu, Adv. Electron. Mater. **6**, 2000079 (2020)
16. M. Wang, Z. Xu, J. Magn. **27**, 7 (2022)
17. Q. Zheng, L. Luo, K.H. Lam, N. Jiang, Y. Guo, D. Lin, J. Appl. Phys. **116**, 184101 (2014)
18. S. Huang, Q. Li, L. Yang, J. Xu, C. Zhou, G. Chen, C. Yuan, G. Rao, Ceram. Int. **44**, 8955 (2018)
19. B.S. Kar, M.N. Goswami, P.C. Jana, P.S. Das, J. Mater. Sci.: Mater. Electron **30**, 2154 (2019)
20. X.-H. Liu, Z. Xu, X.-Y. Wei, X. Yao, J. Am. Ceram. Soc. **91**, 3731 (2008)
21. D. Kan, L. Pálová, V. Anbusathaiah, C.J. Cheng, S. Fujino, V. Nagarajan, K.M. Rabe, I. Takeuchi, Adv. Funct. Mater. **20**, 1108 (2010)
22. S. Pattanayak, R.N.P. Choudhary, P.R. Das, Electron. Mater. Lett. **10**, 165 (2014)
23. S.K. Singh, Thin Solid Films **527**, 126 (2013)
24. F. Zhang, X. Zeng, D. Bi, K. Guo, Y. Yao, S. Lu, Materials **11**, 2208 (2018)
25. T. Wang, X.-L. Wang, S.-H. Song, Q. Ma, Ceram. Int. **46**, 15228 (2020)
26. K. Tsuzuki, K. Sakata, M. Wada, Ferroelectrics **8**, 501 (1974)
27. X. Zhang, Y. Sui, X. Wang, Y. Wang, Z. Wang, J. Alloy. Compds. **507**, 157 (2010)
28. Z.Z. Ma, Z.M. Tian, J.Q. Li, C.H. Wang, S.X. Huo, H.N. Duan, S.L. Yuan, Solid State Sci. **13**, 2196 (2011)
29. M. Mahesh Kumar, S. Srinath, G. S. Kumar, S. V. Suryanarayana, (1998) J. Magn. Magn. Mater. 188, 203
30. D.H. Wang, W.C. Goh, M. Ning, C.K. Ong, Appl. Phys. Lett. **88**, 212907 (2006)
31. A. Kumar, K.L. Yadav, Phys. B: Condens. Matter **405**, 4650 (2010)
32. P. D, D. D, R. M.T, N. Kalarikkal, G. N V, (2021) Appl. Phys. A 127, 293
33. J. Ryu, S. Priya, K. Uchino, H.-E. Kim, J. Electroceram. **8**, 107 (2002)
34. H. Yang, G. Zhang, Y. Lin, J. Alloy. Compds. **644**, 390 (2015)
35. J.W. Liang, X.L. Zhu, L. Zhu, L. Liu, S.Y. Wu, X.Q. Liu, X.M. Chen, J. Alloy. Compds. **901**, 163681 (2022)
36. F. Lin, Q. Yu, L. Deng, Z. Zhang, X. He, A. Liu, W. Shi, J. Mater. Sci. **52**, 7118 (2017)
37. F.M.F. de Groot, M. Grioni, J.C. Fuggle, J. Ghijsen, G.A. Sawatzky, H. Petersen, Phys. Rev. B **40**, 5715 (1989)
38. Z.Y. Wu, S. Gota, F. Jollet, M. Pollak, M. Gautier-Soyer, C.R. Natoli, Phys. Rev. B **55**, 2570 (1997)
39. J.-S. Kang, G. Kim, H.J. Lee, D.H. Kim, H.S. Kim, J.H. Shim, S. Lee, H. Lee, J.-Y. Kim, B.H. Kim, B.I. Min, Phys. Rev. B **77**, 035121 (2008)
40. Y. Ma, P.D. Johnson, N. Wassdahl, J. Guo, P. Skytt, J. Nordgren, S.D. Kevan, J.-E. Rubensson, T. Böske, W. Eberhardt, Phys. Rev. B **48**, 2109 (1993)
41. T. Higuchi, Y.-S. Liu, P. Yao, P.-A. Glans, J. Guo, C. Chang, Z. Wu, W. Sakamoto, N. Itoh, T. Shimura, T. Yogo, T. Hattori, Phys. Rev. B **78**, 085106 (2008)
42. T. Higuchi, T. Hattori, W. Sakamoto, N. Itoh, T. Shimura, T. Yogo, P. Yao, Y.-S. Liu, P.-A. Glans, C. Chang, Z. Wu, J. Guo, Jpn. J. Appl. Phys. **47**, 7570 (2008)
43. P. Ravindran, R. Vidya, A. Kjekshus, H. Fjellvåg, O. Eriksson, Phys. Rev. B **74**, 224412 (2006)
44. K.-T. Ko, M.H. Jung, Q. He, J.H. Lee, C.S. Woo, K. Chu, J. Seidel, B.-G. Jeon, Y.S. Oh, K.H. Kim, W.-I. Liang, H.-J. Chen, Y.-H. Chu, Y.H. Jeong, R. Ramesh, J.-H. Park, C.-H. Yang, Nat. Commun. **2**, 567 (2011)
45. J.B. Neaton, C. Ederer, U.V. Waghmare, N.A. Spaldin, K.M. Rabe, Phys. Rev. B **71**, 014113 (2005)
46. D.H. Douma, R. Ciprian, A. Lamperti, P. Lupo, E. Cianci, D. Sangalli, F. Casoli, L. Nasi, F. Albertini, P. Torelli, A. Debernardi, Phys. Rev. B **90**, 205201 (2014)
47. C.-S. Tu, C.-S. Chen, P.-Y. Chen, H.-H. Wei, V.H. Schmidt, C.-Y. Lin, J. Anthoniappen, J.-M. Lee, J. Eur. Ceram. Soc. **36**, 1149 (2016)
48. D.-Y. Cho, J.-M. Lee, S.-J. Oh, H. Jang, J.-Y. Kim, J.-H. Park, A. Tanaka, Phys. Rev. B **76**, 165411 (2007)
49. T. Higuchi, W. Sakamoto, N. Itoh, T. Shimura, T. Hattori, T. Yogo, Appl. Phys. Express **1**, 011502 (2008)
50. N. Panwar, I. Coondoo, V. Sen, S. K., in Advances in Ceramics - Electric and Magnetic Ceramics, Bioceramics, Ceramics and Environment, edited by C. Sikalidis (InTech, 2011).
51. J. Wei, D. Xue, Appl. Surf. Sci. **258**, 1373 (2011)
52. A. Ablat, R. Wu, M. Mamat, J. Li, E. Muhemmed, C. Si, R. Wu, J. Wang, H. Qian, K. Ibrahim, Ceram. Int. **40**, 14083 (2014)